

Path curvature enhances the flow-induced vibrations of a cylinder without structural restoring force

Rémi Bourguet†

Institut de Mécanique des Fluides de Toulouse, Université de Toulouse and CNRS, Toulouse 31400, France

(Received 20 August 2023; revised 26 September 2023; accepted 4 November 2023)

A cylinder immersed in a current and free to translate along a circular arc is considered to investigate the impact of path curvature on the flow-induced vibrations (FIV) occurring without structural restoring force. Path curvature magnitude (κ , inverse of path radius non-dimensionalized by the body diameter D) is varied from 0 (transverse rectilinear path) to 20, over a wide range of values of the structure to displaced fluid mass ratio, $m^* \in [0.05, 10]$. The exploration is carried out numerically at subcritical and postcritical values of the Reynolds number (Re , based on D and the inflow velocity), i.e. below and above the critical value 47 for the onset of flow unsteadiness when the body is fixed, up to 100. Path curvature triggers a desynchronized regime of the flow–body system in addition to the synchronized regime typical of vortex-induced vibrations, and alters the composition of fluid forcing. The most prominent effect uncovered here is, however, a global enhancement of FIV, with three principal results: (i) vibrations and flow unsteadiness are found to arise at lower subcritical Re along a curved path, down to 19.5 versus 31 for $\kappa = 0$; (ii) the m^* range where substantial responses develop is considerably extended and encompasses the entire interval under study, which contrasts with the narrow band of low m^* identified for $\kappa = 0$; (iii) the vibrations are amplified, +45 % relative to the peak amplitude measured along a rectilinear path at $Re = 100$.

Key words: flow-structure interactions, vortex streets, wakes

1. Introduction

Flow-induced vibrations (FIV) of bluff bodies are omnipresent in nature and in industrial systems. Their impact on the fatigue life of engineering structures, as well as their

† Email address for correspondence: remi.bourguet@imft.fr

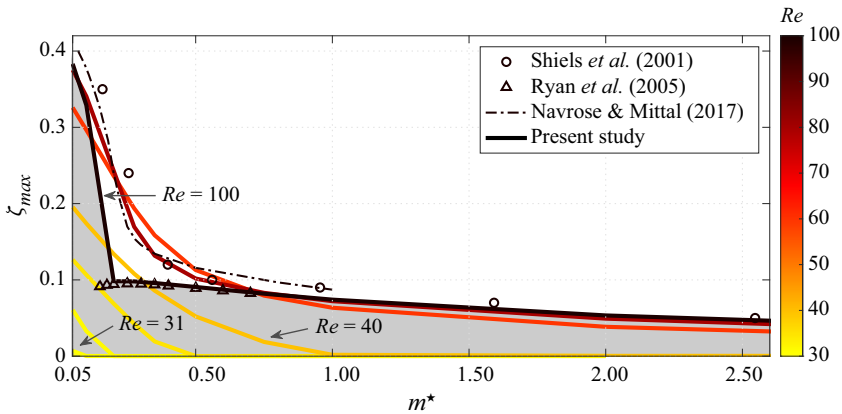


Figure 1. Displacement amplitude of a circular cylinder along a transverse rectilinear path without structural restoring force, as a function of m^* , over a range of subcritical and postcritical Re . The amplitude is defined as the maximum value of the displacement signal fluctuation. The Re value is denoted by line colour. The shaded area highlights the amplitudes reached at $Re = 100$. The present results are compared to those reported at $Re = 100$ by Shiels *et al.* (2001), Ryan *et al.* (2005) and Navrose & Mittal (2017).

fundamental interest as paradigms of fluid–structure interaction, have motivated a number of studies, as reviewed, for example, by Païdoussis, Price & de Langre (2010).

A circular cylinder placed in a cross-current is subjected to vortex-induced vibrations (VIV), a form of FIV that develops through synchronization, or lock-in, between body motion and flow unsteadiness (Williamson & Govardhan 2004). The configuration composed of an elastically mounted cylinder free to translate along a rectilinear path in the direction normal to the current represents a canonical problem to investigate these vibrations. However, VIV also occur when the elastic support is removed, i.e. in the absence of structural natural frequency (Shiels, Leonard & Roshko 2001; Govardhan & Williamson 2002; Ryan, Thompson & Hourigan 2005; Navrose & Mittal 2017). The vibrations encountered in this case exhibit substantial magnitudes only for low values of the structure to displaced fluid mass ratio (m^*). This is visualized in figure 1, where the oscillation amplitude, normalized by the cylinder diameter (D), is plotted as a function of m^* , for different values of the Reynolds number (Re), based on D and the inflow velocity. The peak amplitudes measured for an elastically mounted cylinder, e.g. close to $0.55D$ at $Re = 100$, are not necessarily reached once the restoring force is removed. Under a sinusoidal oscillation assumption that is often reasonable in this context, the responses are actually a subset of those observed for an elastically mounted body. More precisely, they correspond to the subset where the effective added mass due to fluid forcing is negative (Govardhan & Williamson 2002).

Vortex-induced vibrations may appear at Re lower than the critical value 47 associated with the onset of flow unsteadiness for a fixed cylinder. The Re values lower/larger than this critical value are referred to as subcritical/postcritical. Subcritical- Re VIV have been well documented in the elastically mounted body case, where responses were detected down to $Re \approx 20$ (Cossu & Morino 2000; Mittal & Singh 2005; Kou *et al.* 2017; Dolci & Carmo 2019; Boersma *et al.* 2021; Bourguet 2023a). This phenomenon persists along a rectilinear path without structural restoring force, as reported by Ryan *et al.* (2005) at $Re = 40$, and illustrated in figure 1, where vibrations are shown to arise close to $Re = 31$.

The object of this work is to examine the impact of a curved trajectory on the flow–structure system behaviour. It was triggered by a recent study concerning

an elastically mounted cylinder, free to translate along a circular arc within a cross-current at $Re = 100$ (Bourguet 2023b). This study pointed out a major alteration of the vibration properties compared to the rectilinear path configuration, and the emergence of novel interaction regimes. In the present work, the cylinder is also free to translate along a circular arc, whose curvature magnitude (inverse of radius) is a parameter of the system, but without structural restoring force. The behaviour of this system and the possible deviations from the rectilinear VIV depicted in figure 1 remain to be explored; an attempt is proposed here, on the basis of numerical simulations.

Some insights may be gained from prior works analysing the related problem of a tethered cylinder, despite the difference in the nature of body motion, i.e. rotation versus translation (Carberry & Sheridan 2007; Ryan, Thompson & Hourigan 2007). For $m^* < 1$ and postcritical Re , these works emphasized the effect of m^* , with a sharp amplification of the vibrations in the lower- m^* range, as in the rectilinear path case. They also identified a widening of the m^* interval over which substantial vibrations occur, when curvature magnitude is increased. In order to study these trends for the present system and, more generally, to provide a global vision of its behaviour, path curvature magnitude, non-dimensionalized by D , is varied from 0 (rectilinear path) to 20, over a wide range of m^* , 0.05 to 10. The exploration is carried out at both subcritical and postcritical Re , up to 100.

2. Flow–structure system and numerical method

The physical system is schematized in figure 2(a). The circular cylinder of diameter D and mass per unit length M_c is parallel to the z axis and placed in an incompressible uniform cross-current of velocity U , density ρ_f , viscosity μ , aligned with the x axis. The Reynolds number $Re = \rho_f UD/\mu$ is kept below or equal to 100, which ensures that the flow is two-dimensional across the parameter space investigated. This point has been verified in a preliminary phase of the present work, via three-dimensional simulations initialized with three-dimensional flow fields. The two-dimensional Navier–Stokes equations are employed to predict the flow dynamics. The cylinder is free to translate along a circular path of radius R , parallel to the (x, y) plane and centred at the origin of the (x, y, z) frame. The cylinder position is tracked by the angle θ relative to the x axis, referred to as the angular displacement. The physical variables are non-dimensionalized by D , U and ρ_f . The non-dimensional, curvilinear displacement of the cylinder along the circular path is expressed as $\zeta = \theta/\kappa$, where $\kappa = D/R$ is the non-dimensional curvature magnitude. The transverse rectilinear motion configuration corresponds to the limiting case where R tends to infinity ($\kappa = 0$). In this configuration, ζ is the non-dimensional displacement aligned with the y axis. The in-line, transverse and tangential force coefficients are defined as $C_x = 2F_x/(\rho_f DU^2)$, $C_y = 2F_y/(\rho_f DU^2)$ and $C = 2F/(\rho_f DU^2)$, where F_x , F_y and F are the dimensional fluid forces per unit length, parallel to the x and y axes, and to the direction of body motion, respectively. The motion of the cylinder is governed by the equation

$$\ddot{\zeta} = \frac{2C}{\pi m^*}, \quad \text{with } C = -C_x \sin(\kappa \zeta) + C_y \cos(\kappa \zeta). \quad (2.1)$$

The $\dot{}$ symbol designates the non-dimensional time derivative. The structure to displaced fluid mass ratio is defined as $m^* = 4M_c/(\pi\rho_f D^2)$. The system behaviour is examined for $\kappa \in [0, 20]$ and $m^* \in [0.05, 10]$.

Assuming a decoupling of the flow and moving cylinder time scales, a quasi-steady model of C , identified by the superscript qs , and its first-order approximation about

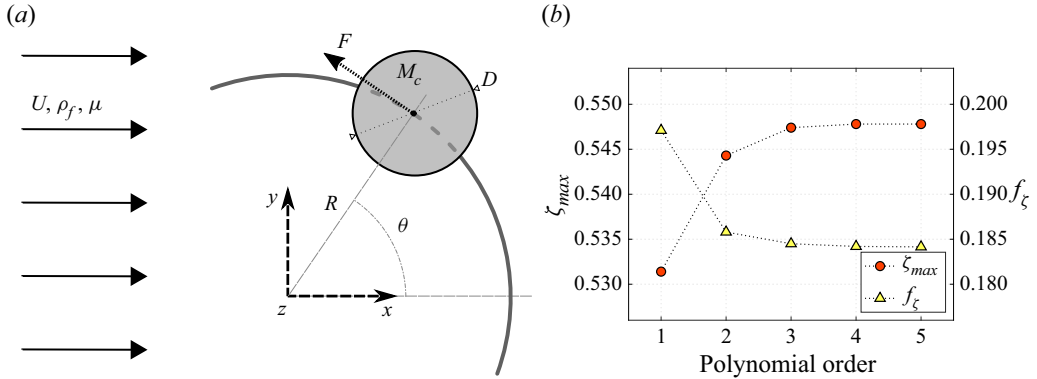


Figure 2. (a) Sketch of the physical system. (b) Curvilinear displacement amplitude (maximum value of signal fluctuation) and frequency as functions of the polynomial order for $(Re, \kappa, m^*) = (100, 0.5, 0.05)$.

$\zeta = \dot{\zeta} = 0$ can be expressed as (Bourguet 2023b)

$$C^{qs} = -\bar{C}_x^f (\dot{\zeta} + \sin(\kappa\zeta)) \sqrt{\dot{\zeta}^2 + 2\dot{\zeta} \sin(\kappa\zeta) + 1} \approx -\bar{C}_x^f (\dot{\zeta} + \kappa\zeta), \quad (2.2)$$

where \bar{C}_x^f is the mean in-line force (or drag) coefficient in the fixed body case. The $\bar{\cdot}$ symbol denotes the time-averaged value. The first term of the approximation (relative to $\dot{\zeta}$) acts as a damping term through which the force tends to oppose body motion. This suggests that no vibration should develop when C is replaced by C^{qs} in the dynamics equation (2.1); this is indeed the case. The second term (relative to ζ) is used to derive a non-dimensional natural frequency

$$f_n = \sqrt{\frac{\bar{C}_x^f \kappa}{2\pi^3 m^*}}, \text{ and the corresponding reduced velocity } U^* = \frac{1}{f_n}. \quad (2.3)$$

Even if the present system behaviour generally departs from the quasi-steady assumption, such modelling may shed some light on the effect of mean fluid forcing, and the above natural frequency will be used in the analysis of the results.

The numerical method is the same as in previous works concerning comparable systems (Bourguet 2023a,b). It is briefly summarized here, and some additional convergence/validation results are presented. The coupled flow–structure equations are solved by the parallelized code Nektar, which is based on the spectral/ hp element method (Karniadakis & Sherwin 1999). A large rectangular computational domain is considered ($350D$ downstream, and $250D$ in front, above and below the cylinder) to avoid any blockage effects. It is discretized in 3975 spectral elements. A no-slip condition is applied on the cylinder surface. A convergence study in the region of peak amplitude vibrations at $Re = 100$ is presented in figure 2(b). The evolutions of the displacement amplitude and frequency (f_ζ), as functions of the spectral element polynomial order, show that an increase from order 4 to 5 has no impact on the results. A polynomial order 4 was selected. A similar procedure was employed to set the non-dimensional time step to 0.0025. In figure 1, the evolution of the displacement amplitude with m^* for $\kappa = 0$ is compared to the evolutions reported by Shiels *et al.* (2001), Ryan *et al.* (2005) and Navrose & Mittal (2017) at $Re = 100$. Some slight differences, which may be attributed to the distinct simulation strategies, can be noted in the location of the amplitude jump. The global trend of the

displacement amplitude and the peak values reached in the low- m^* range are, however, comparable to prior results. This confirms the validity of the present numerical method.

Each simulation is initialized with the established flow past a fixed body at the selected Re . Then the body is released with an initial velocity $\zeta = 0.1$. The analysis is based on time series collected after convergence, over 30 oscillation cycles in the unsteady cases.

3. Impact of path curvature on the system behaviour

The emergence of a vibration region in the (κ, m^*) domain, and its shape and evolution with Re , are examined in § 3.1, together with response amplitude and frequency. Flow–structure interaction mechanisms, including the synchronization regimes, wake patterns and some salient features of fluid forcing, are discussed in § 3.2.

3.1. Vibration region, amplitude and frequency

Within the (κ, m^*) domain investigated, the present simulations show that the onset of vibrations and thus flow unsteadiness may be shifted down to $Re \approx 19.5$, versus $Re \approx 31$ in the rectilinear path configuration (figure 1). As a result, the critical Re value typically reported for an elastically mounted cylinder, close to 20 (e.g. Kou *et al.* 2017), can be reached in the absence of structural restoring force, under the effect of path curvature.

Figure 3(a) represents the curvilinear displacement amplitude in the (κ, m^*) domain at $Re = 20$, i.e. close to vibration onset; $\zeta = 0$ in all cases, and the amplitude is measured as the maximum value of the displacement signal. The vibration region is delimited by dashed lines. Outside this region, the flow–structure system is steady at subcritical Re . As shown in figure 3(e), the vibration region tends to follow the line where the natural frequency induced by the mean drag (2.3) coincides with the Strouhal frequency (St , frequency of flow unsteadiness for a fixed body), or equivalently $U^* = 1/St$. At subcritical Re , the St values are those determined by Kou *et al.* (2017) by triggering the flow: 0.10, 0.11 and 0.115, at $Re = 20$, $Re = 30$ and $Re = 40$, respectively. This trend persists as Re is increased to higher subcritical values, while the vibration region expands continuously (figures 3b,c,f,g). At postcritical Re ($Re = 100$ in figures 3d,h), the cylinder oscillates and the flow is unsteady throughout the parameter space (shaded background). In this case, the region delineated by dashed lines is the area where $\zeta_{max} \geq 0.05$, and the terms ‘vibrations’ and ‘vibration region’ designate the corresponding responses and area. The vibration region remains aligned with the isoline $U^* = 1/St$ ($St = 0.164$ at $Re = 100$). This persistent orientation of the vibration region points out the close link between body and flow dynamics, which is addressed in § 3.2. The isolines $U^* \in \{5, 12\}$ locate the typical U^* range where VIV occur for an elastically mounted body (Williamson & Govardhan 2004). They do not capture the actual limits of the vibration region, but may provide an estimate of its global triangular shape.

Vibrations are encountered over much wider ranges of m^* when the path is curved, compared to the narrow ranges depicted in figure 1 for $\kappa = 0$. Two elements can be noted. First, for any m^* , there always exists an interval of κ where vibrations develop. Second, an increase of κ tends to shift the m^* range towards higher values and simultaneously widens it. This widening is visualized in figures 4(a,b), where the curvilinear and angular displacement amplitudes are represented as functions of m^* for selected κ , at $Re = 100$. The amplitudes measured for $\kappa = 0$ are also plotted, for comparison (grey diamonds). For $\kappa = 5$, the vibration region encompasses most of the m^* range under study.

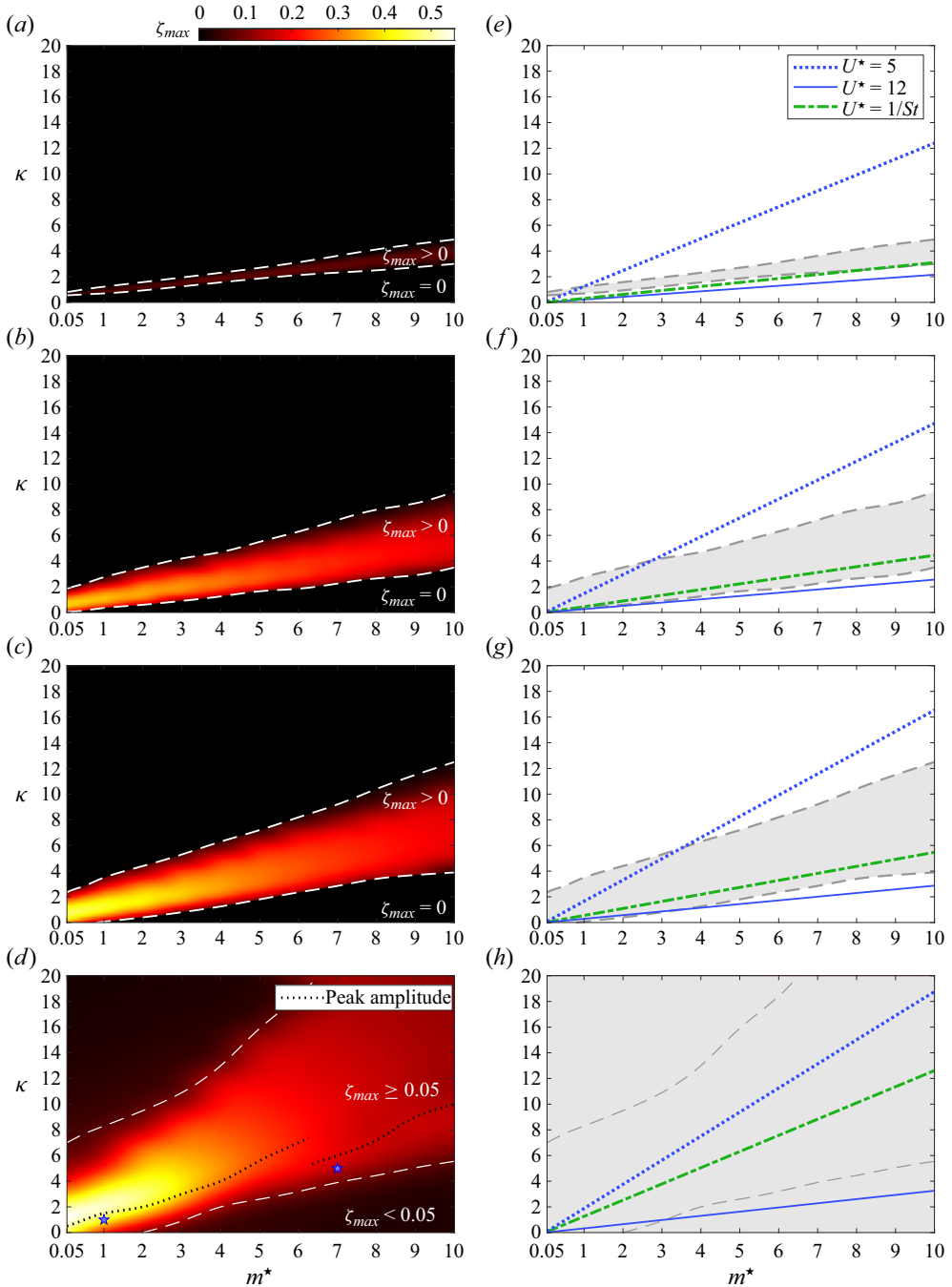


Figure 3. (a–d) Curvilinear displacement amplitude and (e–h) vibration region, as functions of κ and m^* , at (a,e) $Re = 20$, (b,f) $Re = 30$, (c,g) $Re = 40$ and (d,h) $Re = 100$. Dashed lines delimit the area where $\zeta_{max} > 0$ in (a–c,e–g) and $\zeta_{max} \geq 0.05$ in (d,h). In (a–d), the colour levels are the same for all Re . In (d), the location of the peak amplitude as a function of m^* is indicated by a black dotted line. The cases visualized in figure 8 are denoted by blue stars. In (e–h), the shaded area denotes the region where the cylinder exhibits oscillations of any amplitude. The isolines $U^* = 1/St$, $U^* = 5$ and $U^* = 12$ are represented by green dash-dotted, blue dotted and solid lines, respectively. At subcritical Re (e–g), St values are those determined by Kou *et al.* (2017).

FIV along a curved path without structural restoring force

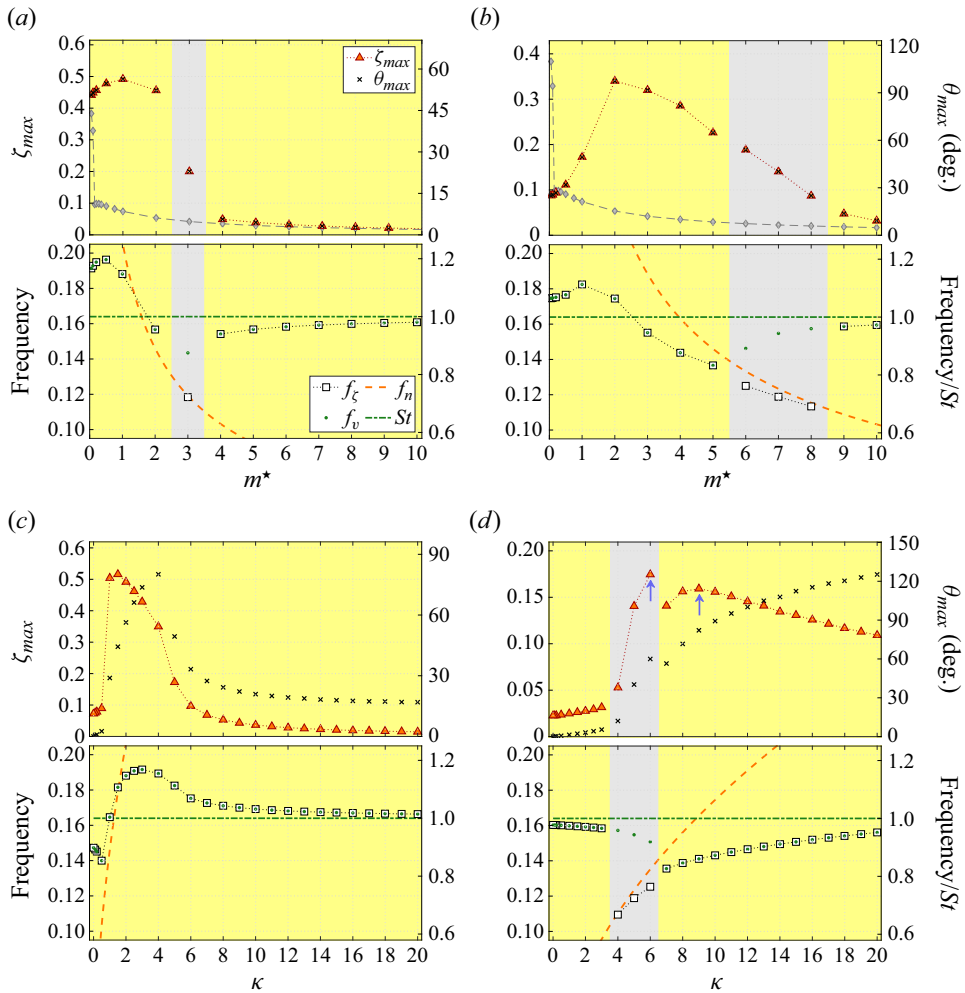


Figure 4. Displacement amplitude (upper plots) and frequency (lower plots) as functions of m^* for (a) $\kappa = 2$ and (b) $\kappa = 5$, and functions of κ for (c) $m^* = 1$ and (d) $m^* = 7$, at $Re = 100$. In the upper plots, both curvilinear (left-hand axis) and angular (right-hand axis) displacement amplitudes are represented. In the lower plots, the displacement frequency is plotted together with flow unsteadiness frequency, the natural frequency (2.3) and St ; a normalization by St is proposed on the right-hand axis. In (a,b), ζ_{max} for $\kappa = 0$ is recalled for comparison (grey diamonds). In (d), blue arrows indicate local peaks of the displacement amplitude. Yellow and grey background colours denote the locked and unlocked regimes, respectively.

The influence of path curvature on vibration amplitude is not monotonic, as illustrated in figures 4(c,d) for selected m^* . However, the peak amplitude at a given m^* is systematically larger for $\kappa > 0$ than the rectilinear response amplitude, including in the low- m^* range. For an elastically mounted body, the increasing evolution of the displacement frequency with κ denotes a reduction of the effective added mass, which may become negative for peak amplitude responses (figure 7 in Bourguet 2023b). This suggests that the subset of responses reached once the elastic support is removed should include the peak amplitude vibrations (Govardhan & Williamson 2002). Such a phenomenon is actually observed: for a fixed κ value larger than a threshold that depends on Re (e.g. $\kappa \approx 0.7$ at $Re = 100$), the peak amplitude attained over the m^* range is the same as that reported for an elastically

mounted body. It should be mentioned that this trend, i.e. reduction of the effective added mass as κ is increased, may also explain the reduction of the critical Re for vibration onset down to values encountered in the elastically mounted body case. The maximum amplitude detected in the present (κ, m^*) domain, $0.55D$ at $Re = 100$ (+45 % compared to the $\kappa = 0$ configuration, where the peak amplitude is $0.38D$), is similar to that measured with an elastic support. A jump in the evolution of the peak amplitude location versus m^* can be noted at $Re = 100$ in [figure 3\(d\)](#) (black dotted line). The two local maxima observed close to the jump are indicated by blue arrows in [figure 4\(d\)](#). This jump reflects the coexistence of two distinct interaction regimes.

When the body oscillates, the displacement spectrum is dominated by a single frequency, f_ζ . A general view of f_ζ over the (κ, m^*) domain, at $Re \in \{20, 30, 40, 100\}$, is presented in [figures 5\(a–d\)](#). For $\kappa = 0$, when vibrations develop ($Re = 40$ and 100), their frequency is restrained to a narrow range and is always lower than St . The frequency range explored by the body once it vibrates along a curved path is considerably extended and includes St (blue dotted line), for example at $Re = 100$, $f_\zeta \in [0.11, 0.198]$ versus $f_\zeta \in [0.132, 0.161]$ for $\kappa = 0$. The f_ζ range tends to increase with Re . A distinct region of low frequency relative to St can be identified close to the lower edge of the vibration region at $Re = 100$ (white dots in [figure 5d](#)). As discussed in the next subsection, this region relates to the emergence of a specific regime of the flow–structure system, under the influence of path curvature.

3.2. Flow–structure interaction mechanisms

In order to visualize the connection between cylinder and flow dynamics, the displacement frequency is represented in [figure 4](#), together with the dominant frequency of flow unsteadiness, f_v , issued from the time series of the transverse component of flow velocity (v) sampled $10D$ downstream of the body. These plots depict two states of flow–body synchronization, where f_ζ and f_v are either equal or incommensurable. They are the two possible unsteady states encountered in the parameter space, as illustrated in [figures 5\(e–h\)](#), where the response amplitude is plotted as a function of the flow/body frequency ratio f_v/f_ζ , for all simulated cases, at $Re \in \{20, 30, 40, 100\}$. The associated regimes are named locked and unlocked, and denoted by yellow and grey background colours, respectively, in [figure 4](#).

The locked regime ($f_\zeta = f_v$) corresponds to the lock-in condition usually reported for VIV of elastically mounted cylinders (Williamson & Govardhan 2004). In the present configuration and up to the highest Re considered ($Re = 100$), this is the only unsteady regime encountered for $\kappa = 0$ (black crosses in [figures 5\(g,h\)](#); $\zeta = 0$ for $\kappa = 0$ at $Re = 20$ and 30). At subcritical Re , this is also the only unsteady regime appearing for $\kappa > 0$. The locked regime may be associated with deviations from f_n and St ([figure 4](#)). Such deviations are quantified over the (κ, m^*) domain in [figures 6](#) and [7](#), respectively, via amplitude versus frequency ratio plots. The large-amplitude responses often develop relatively close to f_n , but substantial departures, mainly oriented towards lower frequencies ($f_\zeta < f_n$), can occur. The frequency range may vary from -20% to $+35\%$ of St , depending on Re . At $Re = 100$, it follows approximately the boundaries of the wake synchronization region determined by Koopmann (1967) for forced rectilinear oscillations (red dotted lines in [figure 7d](#)). As previously mentioned, the system frequency is lower than St for $\kappa = 0$ (black crosses).

The unlocked regime (f_ζ and f_v incommensurable) resembles the desynchronized condition observed for VIV at higher Re , beyond the lock-in range. It does not appear at subcritical Re . At $Re = 100$, it emerges for $\kappa > 1$. Its location in the (κ, m^*) domain is

FIV along a curved path without structural restoring force

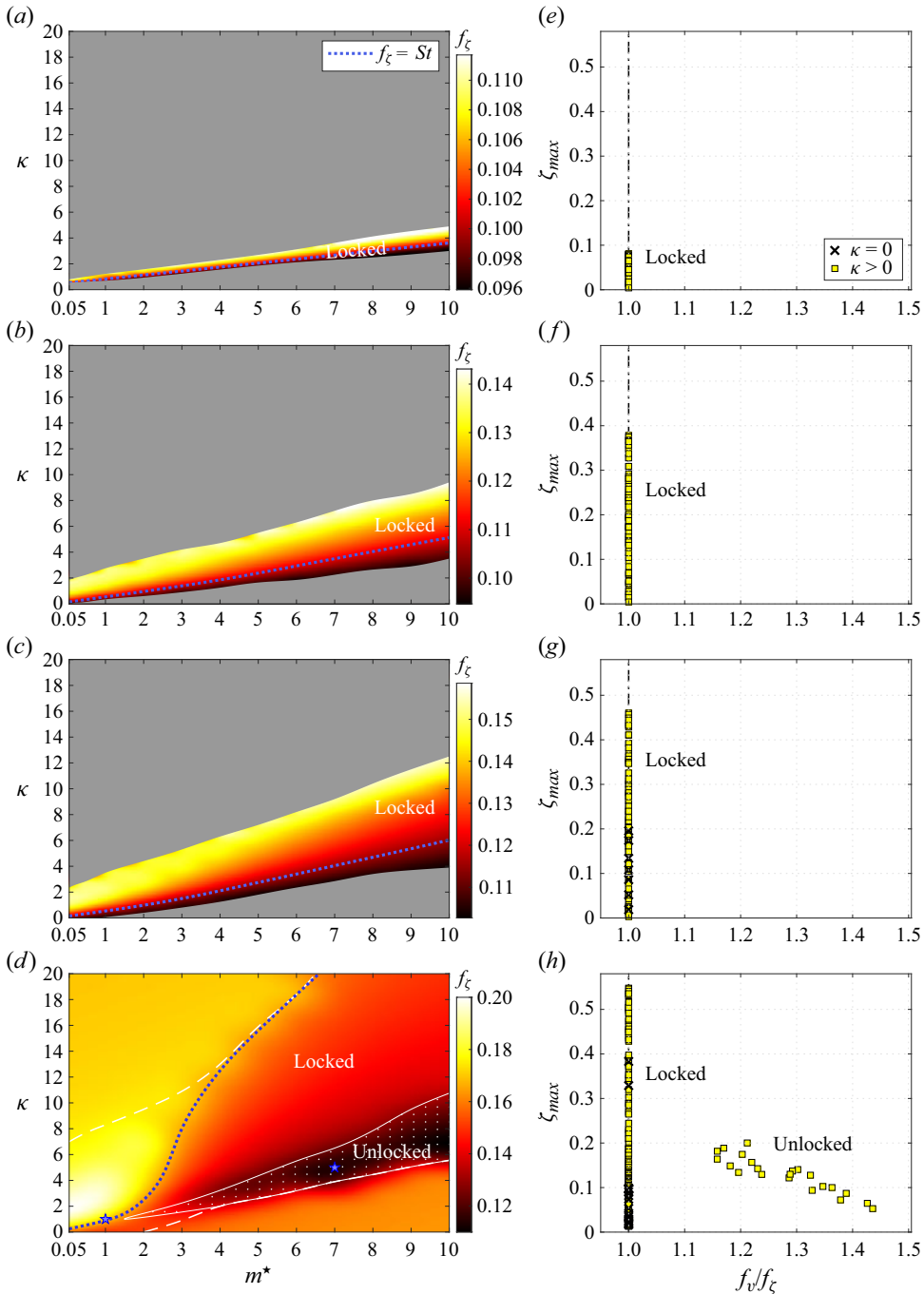


Figure 5. (a–d) Displacement frequency as a function of κ and m^* , and (e–h) curvilinear displacement amplitude as a function of the ratio between the flow unsteadiness and body displacement frequencies, at (a,e) $Re = 20$, (b,f) $Re = 30$, (c,g) $Re = 40$ and (d,h) $Re = 100$. In (a–d), the isoline $f_\zeta = St$ is represented by a blue dotted line. In (d), white dashed lines delimit the area where $\zeta_{max} \geq 0.05$. The unlocked regime region is indicated by white dots and delineated by a thin white line. The cases visualized in figure 8 are denoted by blue stars. In (e–h), the frequency ratio 1 is specified by a black dash-dotted line. In (g,h), the results obtained for $\kappa = 0$ are represented by black crosses; $\zeta = 0$ for $\kappa = 0$ at $Re \in \{20, 30\}$.

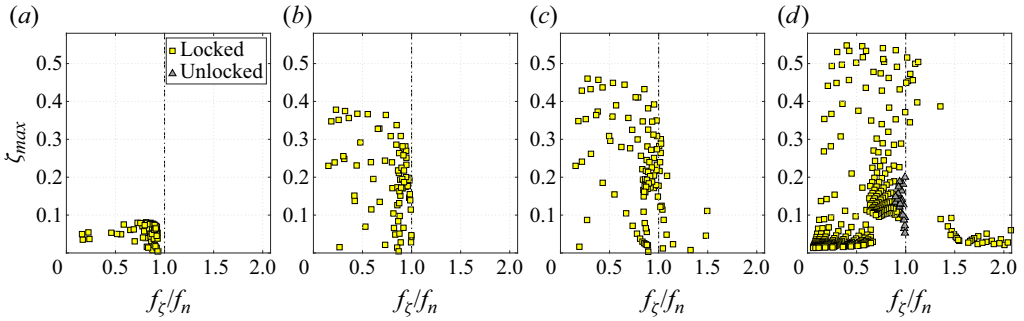


Figure 6. Curvilinear displacement amplitude as a function of the ratio between the body displacement and natural frequencies at (a) $Re = 20$, (b) $Re = 30$, (c) $Re = 40$ and (d) $Re = 100$. The frequency ratio 1 is specified by a black dash-dotted line. Distinct symbols are used to designate the locked and unlocked regime cases.

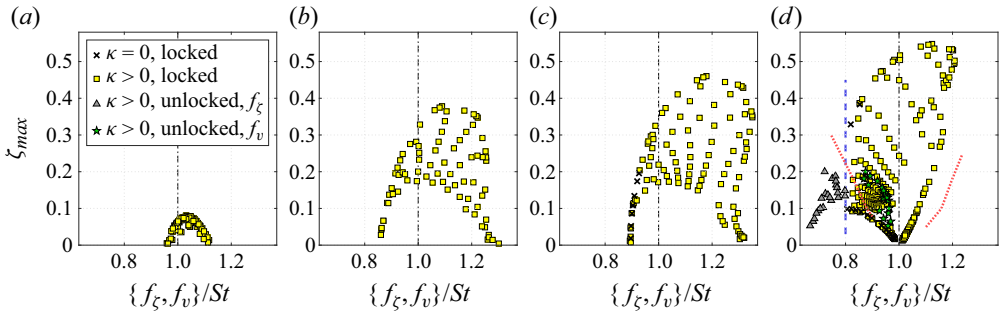


Figure 7. Curvilinear displacement amplitude as a function of the ratio between the body displacement/flow unsteadiness and Strouhal frequencies at (a) $Re = 20$, (b) $Re = 30$, (c) $Re = 40$ and (d) $Re = 100$. The frequency ratio 1 is specified by a black dash-dotted line. In (c,d), the results obtained for $\kappa = 0$ are represented by black crosses; $\zeta = 0$ for $\kappa = 0$ at $Re \in \{20, 30\}$. In (d), a blue dashed line visualizes the threshold below which flow–body synchronization ceases, i.e. the unlocked regime; f_ζ and f_v are plotted in this case. Red dotted lines delimit the synchronization region reported by Koopmann (1967) under forced transverse oscillations at $Re = 100$.

indicated by white dots in figure 5(d); the locked regime is established over the rest of the domain. The unlocked regime is associated with a range of moderate response amplitudes, $\zeta_{max} \in [0.05, 0.2]$, and flow/body frequency ratios varying from 1.15 to 1.45 (figure 5h). The frequency plots in figure 4 suggest that in the unlocked regime, the body oscillates very close to f_n , possibly far from St compared to f_v . These observations are confirmed in figures 6(d) and 7(d). In particular, the displacement frequency is found to remain lower than a threshold located at approximately $0.8St$ (blue dashed line in figure 7d).

The dynamics of the flow–structure system is periodic in the locked regime. In the unlocked regime, the body displacement and flow velocity signals are close to periodic. Yet the presence of incommensurable components, at f_v in the ζ spectrum and at f_ζ in the v spectrum, results, despite their limited contributions, in modulations of the temporal evolutions. Selected time series in cases representative of each regime are plotted in figure 8, together with instantaneous visualizations of the wake. Across the entire parameter space, and regardless of Re , f_v corresponds to the shedding of a pair of counter-rotating vortices. Therefore, a pair of vortices is formed per oscillation cycle in

FIV along a curved path without structural restoring force

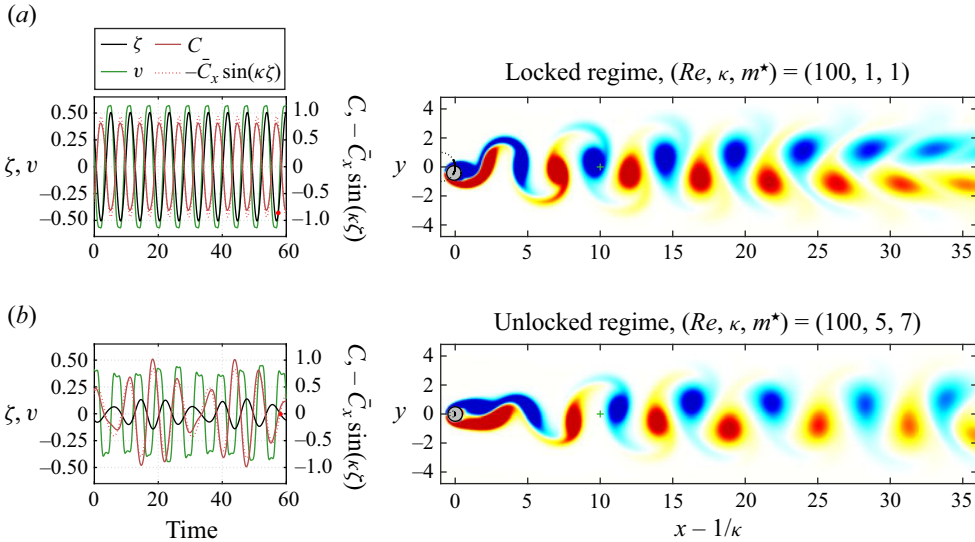


Figure 8. Selected time series of the curvilinear displacement, transverse component of flow velocity, tangential force coefficient and mean drag contribution to the tangential force coefficient, and instantaneous isocontours of spanwise vorticity ($\omega_z \in [-0.8, 0.8]$), for (a) $(\kappa, m^*) = (1, 1)$ (locked regime) and (b) $(\kappa, m^*) = (5, 7)$ (unlocked regime), at $Re = 100$. The time instant visualized in the right-hand plot is indicated by a red dot in the ζ time series. The circular path and trajectory of the cylinder centre are represented by black dashed and solid lines. The sampling point of flow velocity is denoted by a green cross. Positive/negative vorticity values are plotted in red/blue.

the locked regime. In the unlocked regime, based on flow/body frequency ratio ($f_v/f_\zeta \in [1.15, 1.45]$), between 2.3 and 2.9 vortices are shed per oscillation cycle. In all cases, the organization of the wake remains close to the von Kármán street occurring in the fixed body configuration. The aperiodic dynamics of the system in the unlocked regime is, however, betrayed by subtle variations in the streamwise distance between consecutive vortices and in their alignment. It is recalled that the unlocked regime does not develop for $\kappa = 0$: the reported alteration of wake regularity is an effect of path curvature.

The amplification of the mean drag associated with the emergence of vibrations is enhanced by path curvature. For example, at $Re = 100$, it reaches +65% relative to $\bar{C}_x^f = 1.32$ close to $\kappa = 1.5$, versus +15% for $\kappa = 0$. In the absence of structural restoring force and damping, for periodic responses such as those encountered in the locked regime, the components of C and ζ at f_ζ are in phase opposition. This phasing state persists in the unlocked regime, as shown in figure 8, where C time series are represented for both regimes. For $\kappa = 0$, the drag is not involved in C and is thus disconnected from body excitation. In contrast, it may play a significant role once the path is curved. The mean drag contribution ($-\bar{C}_x \sin(\kappa \zeta)$) actually becomes predominant over most of the vibration regions identified in figure 3, as illustrated by its proximity with C in figure 8. As a result, body excitation, i.e. positive $C\dot{\zeta} \approx -\bar{C}_x \dot{\zeta} \sin(\kappa \zeta) = \bar{C}_x \dot{\zeta}_x$, where $\dot{\zeta}_x$ is the in-line velocity of the body, occurs mainly during downstream motion.

4. Conclusions

In order to investigate the influence of path curvature on the flow-induced vibrations (FIV) arising without structural restoring force, a cylinder free to translate along a circular

trajectory within a current was considered for $\kappa \in [0, 20]$ and $m^* \in [0.05, 10]$. The study was carried out numerically, at subcritical and postcritical Re up to 100.

The location and shape of the vibration region in the (κ, m^*) domain may be estimated based on a natural frequency f_n , emerging from the combination of the mean drag and path curvature. At subcritical Re and over most of the vibration region at postcritical Re , the frequencies of body motion and flow unsteadiness coincide, as in the transverse rectilinear path configuration ($\kappa = 0$). In addition to this locked regime, path curvature triggers a second regime at postcritical Re , for $\kappa > 1$ at $Re = 100$. In this second regime, called unlocked and associated with responses of moderate amplitudes occurring very close to f_n , the body and the flow oscillate at incommensurable frequencies. The frequency range explored by the flow–body system is considerably extended when the cylinder vibrates along a curved path. It includes St , which is not the case for $\kappa = 0$. The organization of the wake remains, however, comparable to the von Kármán street observed downstream of a fixed cylinder, with subtle irregularities in the unlocked regime. Along a curved trajectory, it appears that the contribution of the mean drag to body excitation may become predominant, while it does not participate in energy transfer for $\kappa = 0$.

Path curvature results in a global enhancement of FIV. Three facets of this enhancement have been pointed out. First, the Re range where vibrations and flow unsteadiness develop is extended down to $Re \approx 19.5$, a subcritical value typically reported for elastically mounted bodies, versus $Re \approx 31$ for $\kappa = 0$. Second, substantial vibrations may be encountered, over an interval of κ , for any m^* , and the vibration region along the m^* axis tends to widen as κ is increased. This contrasts with the narrow band of low m^* identified for a rectilinear trajectory. Third, the peak amplitude of vibration detected for $\kappa > 0$, at a given m^* , is always larger than the amplitude measured for $\kappa = 0$. At $Re = 100$, the maximum amplitude is $0.55D$, i.e. +45 % compared to the rectilinear path configuration.

Different phenomena, depicted in this paper for a relatively specific system, may also be encountered in a variety of flow–structure interaction problems where the body moves along a curved path, for example in tethered or pivoted body systems. Some elements are summarized hereafter.

Proximity with the elastically mounted body case. In the rectilinear path configuration, the behaviour of the system without structural restoring force deviates noticeably from that observed when the body is elastically mounted. Path curvature is found to reduce this deviation. In particular, the critical values of Re for the onset of vibrations/flow unsteadiness and the peak amplitudes of body responses, with and without structural restoring force, become comparable.

Role of the mean drag. When body motion occurs along a curved path, the drag plays a role in flow–body interaction, which is not the case in the rectilinear path configuration. Its mean contribution may dominate the tangential force and the energy transfer between the flow and the moving body. Moreover, combined with path curvature, the mean drag introduces a natural frequency in the system.

Natural frequency. In the absence of elastic restoring force, the structure has no intrinsic natural frequency. The present results emphasize the significance of the natural frequency that arises spontaneously when the body is placed in a current, under the joint effects of the mean drag and path curvature: it determines the location of the vibration region in the parameter space and drives the global evolution of the vibration frequency.

Funding. This work was performed using HPC resources from CALMIP (grants 2022-P1248 and 2023-P1248). This research received no specific grant from any funding agency, or commercial or not-for-profit sectors.

Declaration of interests. The author reports no conflict of interest.

Author ORCIDs.

 Rémi Bourguet <https://orcid.org/0000-0001-8079-3140>.

REFERENCES

- BOERSMA, P.R., ZHAO, J., ROTHSTEIN, J.P. & MODARRES-SADEGHI, Y. 2021 Experimental evidence of vortex-induced vibrations at subcritical Reynolds number. *J. Fluid Mech.* **922**, R3.
- BOURGUET, R. 2023a Forced rotation enhances cylinder flow-induced vibrations at subcritical Reynolds number. *J. Fluid Mech.* **955**, R3.
- BOURGUET, R. 2023b Flow-induced vibrations of a cylinder along a circular arc. *J. Fluid Mech.* **954**, A7.
- CARBERRY, J. & SHERIDAN, J. 2007 Wake states of a tethered cylinder. *J. Fluid Mech.* **592**, 1–21.
- COSSU, C. & MORINO, L. 2000 On the instability of a spring-mounted circular cylinder in a viscous flow at low Reynolds numbers. *J. Fluids Struct.* **14**, 183–196.
- DOLCI, D.I. & CARMO, B.S. 2019 Bifurcation analysis of the primary instability in the flow around a flexibly mounted circular cylinder. *J. Fluid Mech.* **880**, 1–11.
- GOVARDHAN, R. & WILLIAMSON, C.H.K. 2002 Resonance forever: existence of a critical mass and an infinite regime of resonance in vortex-induced vibration. *J. Fluid Mech.* **473**, 147–166.
- KARNIADAKIS, G.E. & SHERWIN, S. 1999 *Spectral/hp Element Methods for CFD*, 1st edn. Oxford University Press.
- KOOPMANN, G.H. 1967 The vortex wakes of vibrating cylinders at low Reynolds numbers. *J. Fluid Mech.* **28**, 501–512.
- KOU, J., ZHANG, W., LIU, Y. & LI, X. 2017 The lowest Reynolds number of vortex-induced vibrations. *Phys. Fluids* **29**, 041701.
- MITTAL, S. & SINGH, S. 2005 Vortex-induced vibrations at subcritical *Re*. *J. Fluid Mech.* **534**, 185–194.
- NAVROSE, & MITTAL, S. 2017 The critical mass phenomenon in vortex-induced vibration at low *Re*. *J. Fluid Mech.* **820**, 159–186.
- PAÏDOUSSIS, M.P., PRICE, S.J. & DE LANGRE, E. 2010 *Fluid–Structure Interactions: Cross-Flow-Induced Instabilities*. Cambridge University Press.
- RYAN, K., THOMPSON, M.C. & HOURIGAN, K. 2005 Variation in the critical mass ratio of a freely oscillating cylinder as a function of Reynolds number. *Phys. Fluids* **17**, 038106.
- RYAN, K., THOMPSON, M.C. & HOURIGAN, K. 2007 The effect of mass ratio and tether length on the flow around a tethered cylinder. *J. Fluid Mech.* **591**, 117–144.
- SHIELS, D., LEONARD, A. & ROSHKO, A. 2001 Flow-induced vibration of a circular cylinder at limiting structural parameters. *J. Fluids Struct.* **15**, 3–21.
- WILLIAMSON, C.H.K. & GOVARDHAN, R. 2004 Vortex-induced vibrations. *Annu. Rev. Fluid Mech.* **36**, 413–455.